



Global Stratospheric Impact of Solid Rocket Motor Launchers

Prepared for:

U.S. Air Force Space and Missile Systems Center
Environmental Management Branch
SMC/AXFV

under
Contract F09603-95-D-0176-0007

Prepared by:

Malcolm Ko, Run-Lie Shia, Debra Weisenstein, Jose Rodriguez, Nien-Dak Sze
Atmospheric and Environmental Research, Inc.
Cambridge, MA

John R. Edwards, Daniel Pilson
Environmental Management Branch

Peter D. Lohn, and Tyrrel W. Smith, Jr.
TRW Space & Electronics Group

Submitted by:

TRW Space & Electronics Group

30 September 1999



Global Stratospheric Impact of Solid Rocket Motor Launchers

Prepared for:

U.S. Air Force Space and Missile Systems Center
Environmental Management Branch
SMC/AXFV

under

Contract F09603-95-D-0176-0007

Prepared by:

Malcolm Ko, Run-Lie Shia, Debra Weisenstein, Jose Rodriguez, Nien-Dak Sze
Atmospheric and Environmental Research, Inc.
Cambridge, MA

John R. Edwards, Daniel Pilson
Environmental Management Branch

Peter D. Lohn, and Tyrrel W. Smith, Jr.
TRW Space & Electronics Group

Submitted by:

TRW Space & Electronics Group

Approved by:

John J. Lamb, Ph.D.
Program Manager

30 September 1999

Abstract

We used the GISS/Harvard/UCI 3-D CTM on the AER computer platform to perform a number of simulations to obtain the surface area from accumulation of Al_2O_3 particulates from solid rocket motors (SRM), orbital debris, and meteorites. In the calculation, the initial size distribution of the particulates emitted by SRM is represented by a tri-modal distribution with bulk density of 1.7 gm/cm^3 . It is assumed that particles do not interact with each other so that particles in each size bin will evolve independently. Particles from orbital debris and meteorites are assumed to be $1 \text{ }\mu\text{m}$ size particles with bulk density of 4.7 gm/cm^3 and 2.0 gm/cm^3 , respectively. Apart from the large-scale transport, particle distributions are also affected by sedimentation. In addition, we consider the effect of removal of the particles by collision with the background sulfate layer.

The calculated surface area of Al_2O_3 particulates from SRM, with an input of 1120 tons/yr, is between $1\text{-}4 \times 10^{-4} \text{ }\mu\text{m}^2/\text{cm}^3$ in the lower stratosphere with the largest values occurring at northern high latitudes. The assumed input from orbital debris and meteorites are much smaller at 10 tons/yr and 30 ton/yrs respectively. The calculated surface areas are also much smaller at $10^{-6} \text{ }\mu\text{m}^2/\text{cm}^3$ and $10^{-5} \text{ }\mu\text{m}^2/\text{cm}^3$ respectively. These values are to be compared with the sulfate surface area of $0.5\text{-}1.0 \text{ }\mu\text{m}^2/\text{cm}^3$ in the lower stratosphere during non-volcanic conditions, and value of $20 \text{ }\mu\text{m}^2/\text{cm}^3$ one year after the Pinatubo eruption.

The accumulation of Al_2O_3 particulates in the atmosphere may affect ozone via the heterogeneous reaction $\text{ClONO}_2 + \text{HCl} \rightarrow \text{HNO}_3 + \text{Cl}_2$ that converts ClONO_2 and HCl , chlorine reservoir species, into the more active form that will deplete ozone in the presence of sunlight. However, due to the very small Al_2O_3 surface areas calculated, ozone depletion on the global scale is very small. The impact on the stratospheric sulfate aerosol layer is likely to be small over most of the stratosphere, but the impact cannot be evaluated with accuracy at this time.

Table of Content

Section 1: Description of the 3-D CTM	3
1.1 Model Resolutions and Winds	3
1.2 Performance on the AER Platform	4
1.3 Numerical Experiments of Inert Tracer from Rocket Launches	5
Section 2: Overall Approach	7
2.1 Sedimentation Velocity	7
2.2 Removal by Collision with Sulfate Aerosol	8
2.3 Model Simulations	9
Section 3: Particulates from Solid Rocket Motors	10
3.1 Description of Source Function	10
3.2 Model Simulations	12
3.3 Residence Times of Al ₂ O ₃ Particulate from SRM	13
3.4 Surface Area of Al ₂ O ₃ Particulate from SRM	14
Section 4: Input from Meteorites	16
Section 5: Input from Orbital Debris	18
Section 6: Estimate of the effects from Al₂O₃ particulate on stratospheric ozone and the sulfate layer	19
References	21

Section 1: Introduction

Description of the global dispersions of materials emitted by rockets involves simulations at different spatial and temporal scales. The primary interest in this study is the global scale. For the purpose of this study, we will assume that emitted materials from the rocket are dispersed instantaneously and uniformly through the model grid box (see below for the size of the model grid-box).

Calculations in this report were performed using the 21 layer GISS/Harvard/UCI Three-Dimensional Chemistry Transport Model (3-D CTM). This model is upgraded from the 9 layer Harvard/GISS 3-D CTM for the troposphere, which has been documented by Prather *et al.*, [1987]. The 21 layer model has been described in detail in Prather *et al.*, [1990a]. Both models have been used to study a variety of problems in the atmosphere, which include CFC simulations (Prather *et al.*, [1987]), the effects of debris from meteors on the Antarctic ozone (Prather and Rodriguez [1988]), the dynamical dilution of the Antarctic ozone hole (Prather *et al.*, [1990a]), the Space Shuttle's impact on the stratosphere (Prather *et al.*, [1990b]), the trend and annual cycle in stratospheric CO₂ (Hall and Prather [1993]), the seasonal evolution of N₂O, O₃, and CO₂ (Hall and Prather, 1995) and trace-tracer correlation in the stratosphere (Avallone and Prather [1997]).

1.1 Model Resolutions and Winds

A. Model resolution and range

This is a global model with a resolution of 7.83° (latitude) x 10° (longitude) x 21 layers (altitude). In the longitudinal direction, there are 36 boxes (I=1 to 36) with 10 degree longitudinal width. The I=1 box is centered on the date line (180E = 180W) and I increases eastward. In the latitudinal direction, there are 24 boxes (J=1 to 24) from pole to pole with the J=1 box at the South Pole. The 7.83° width is equal to 180°/23 to get an 'over-the-pole' box of the same length as the other boxes. In the vertical direction, there are 21 layers (L=1 to 21). The bottom 9-layers (L=1 is near the surface) are pure σ layers with the pressure at the edge defined by:

$$p(\text{edge}) = \sigma * (P_{\text{surf}} - 100 \text{ mbar}) + 100 \text{ mbar}$$

with $\sigma = 1.00, 0.973, 0.938, 0.887, 0.788, 0.638, 0.460, 0.278, 0.117, 0.0$. The top 12-layers (from 100 mbar up) are at fixed pressure levels, with

$$p(\text{edge}) = 100.0, 46.41, 21.54, 9.998, 4.641, 2.155, 1.000, 0.464, 0.216, \\ 0.100, 0.0466, 0.0215, 0.0022 \text{ mbar.}$$

B. Transport numerics

The Prather advection scheme (*Prather [1986]*), which conserves second moments of tracer distribution, is used in the model. Although this scheme requires more CPU time and more storage space to run, previous work (*see Shia et al., [1990]*) shows it does a good job for simulating advection of tracers with large gradients. The only (explicit) diffusion included in the model is the horizontal diffusion caused by convection.

C. Meteorological fields

The 3-D CTM is driven by the meteorological fields from the GISS-II general circulation model (GCM) with 23-layers, GCMAM, that includes basic GISS-II GCM physics for the 9-layer model with gravity wave drag for the stratosphere and other improvements (*Rind et al., [1990], Prather et al., [1993]*). The top 3 layers have been combined into a single layer to drive the 21-layer CTM. We have received the meteorological fields generated by GCMAM every 8 hours for 365 days. The data are used repeatedly every year.

1.2 Performance on the AER platform

We received from Prof. Prather of UCI a CD-ROM, which includes the FORTRAN source code for the 21 layer GISS/Harvard/UCI 3-D CTM and also the inputs and outputs for two sample runs for testing (*Prather, private communication, [1997]*). The code has been ported on to a SGI Power Challenge machine at AER. First, the two sample runs were repeated. Both runs simulate N₂O and NO_y distributions in the

atmosphere, one for 7 years and one for 1 week. The shorter run has more detailed diagnostic output, including the global budget, the tendency, the concentrations of N₂O and NO_y. Our model outputs are the same as those calculated at UCI, which came with the CD-ROM. The CPU time (one processor) for the 7 year run on the SGI machine is about 9 hours.

In order to use this model to simulate the transport of an inert tracer, like the emissions from rockets or deorbiting space debris, all the sources/sinks in the model have been deactivated. For an inert tracer, if there is no deposition to the surface the total mass of the tracer should be conserved. We tested the mass conservation and after one year model run the total mass of the inertial trace is conserved closed to the machine accuracy (less than 10⁻¹⁰).

1.3 Numerical Experiments Simulating Accumulation of Chlorine from Rocket Launches

We performed two experiments to simulate the distributions of chlorine emitted by rocket launches. The source term in our experiment corresponds to the chlorine emissions from nine launches of the Space Shuttle yearly. The source is located above Cape Canaveral, Florida (29°N, 80°W) and its vertical distribution is taken from Prather *et al.*, [1990b]. The inputs are concentrated in northern mid-latitudes and the magnitudes, in mixing ratio unit, are largest around 30-40 km region. In the simulation, the mixing ratio of the tracers in the lowest 3 layers is continuously set to zero to simulate efficient washout to the ground.

In the first experiment, the emissions are put into the model every 40 days starting at day 40 every year to represent each individual launch. The input of Cl into the stratosphere is 68 ton for every launch and the total inputs of Cl every year is 68 ton x 9 times/year = 612 ton/year. After 10 years, the tracer distribution reaches an annual repeating steady state. The total calculated Cl content in the atmosphere is 1413 ton, which means that the residence time of Cl from Space Shuttle launches is about $1413[\text{ton}] / 612[\text{ton/year}] = 2.3$ years. The zonally averaged Cl mixing ratio distribution in the steady state for 4 seasons is plotted in Figure 1A. Figure 1A shows the dispersion of the input Cl downward and upward from this region and also across the equator into the Southern Hemisphere. To assess the effect of the intermittent source, we performed a second experiment in which the emissions from the same nine launches were spread

uniformly through the year. The results from this experiment are shown in Figure 1B. Comparison of Figures 1A and 1B indicates that there is no significant difference between the calculated distributions. Since the exact timing of the launches are not fixed, we will use the continuous source function in the rest of the calculations

The seasonal variability of the transport is demonstrated in Figures 1A and 1B. Due to the weaker transport in later summer and early fall in the Northern Hemisphere, the input CI tends to accumulate the most in summer and fall in the source region, a maximum of the CI mixing ratio of 11 pptv. Results from Prather *et al.*, [1990b] is shown in figure 1C for comparison. The differences between Figures 1B and 1C are caused by the differences in magnitudes and locations of source input (nine shuttle launches versus nine shuttle launches plus six Titan launches).

Section 2: Overall Approach

In this project, we will treat the particulate from the various sources as non-interacting particles. It is important to list the assumptions, along with the rationales, that will be made in this study.

The main purpose of the study is to provide an estimate of the effect on stratospheric ozone from reactions that may occur on the surfaces of the particles from rocket exhaust and space debris. Since the reaction rates are proportional to the surface area, we can obtain an upper limit on the effects by maximizing the surface area. In the atmosphere, particles may coagulate to form larger particles. Coagulation will reduce the surface area (larger particles have a smaller surface to volume ratio). Larger particles have larger sedimentation velocity and are removed more rapidly from the atmosphere. Thus ignoring coagulation in the simulation will maximize both the surface area density and mass density of the particles in the atmosphere. Although there are indications that H_2SO_4 may not readily condense on Al_2O_3 particles, we feel that it is nonetheless useful to estimate the effect of the particles as condensation nuclei for sulfate aerosol. Again, in this case, smaller particles are more efficient as condensation nuclei. For these reasons, we decided that we will treat the emitted particles as non-interacting and ignore coagulation in the calculations. Once the emitted particles are dispersed to the size of the model grid box, number densities will be low enough that coagulation between Al particles will not be an important process anyway.

2.1 Sedimentation Velocity

Sedimentation is an important process for atmospheric particles, affecting their residence time and vertical distribution. Our treatment of gravitational sedimentation follows Kasten [1968]. The falling speed (w_{sed}) of spherical particles due to gravity is a function of particle density (ρ_{bulk}), radius (D), air viscosity (η) and mean free path (λ):

$$w_{\text{sed}} = \frac{2}{9} \left| \frac{\rho_{\text{bulk}} D^2 g}{\eta} \right| \left[1 + \frac{\lambda}{D} \left(1.249 + 0.42 \exp \left\{ -\frac{0.87 D}{\lambda} \right\} \right) \right]. \quad (1)$$

Air viscosity is a function of ambient temperature, while mean free path is a function of both temperature and atmospheric pressure. Particles between 0.02 μm and 0.1 μm radius

do not settle appreciable in the lower stratosphere, but are influenced by gravitational sedimentation at higher altitudes. Particles greater than 0.1 μm radius are influenced by sedimentation at all altitudes, and particles greater than 1.0 μm radius are rapidly removed from the stratosphere. The sedimentation velocity, defined in Equation (1), is plotted as a function of the particle size in Figure 2. The three curves represent the sedimentation velocity at 20° N around 20 km, 30 km, and 40 km respectively. At the same altitude, bigger particles have larger sedimentation velocity because, relatively speaking, the air resistance is smaller for the bigger particles. For particles with the same size, the sedimentation velocity is larger at higher altitude because the thinner air at higher altitude provides less friction for the particles. The sedimentation velocity is almost 20 times larger at 40 km than that at 20 km. Typical magnitudes of the vertical advection velocity from the large scale circulation are 0.05 km/day at 20 km, and 0.1 km/day at 40 km. Thus sedimentation is important only for particles larger than 0.1 μm .

2.2 Removal by collision with sulfate aerosol

A first order loss rate for each size bin of aluminum particles can be generated using the following formula:

$$\frac{\partial n_j}{\partial t} = n_j \sum_{k \geq j} K_{jk} N_k^{\text{sulfate}} \quad (2)$$

where n_j represents the number density of Al_2O_3 particles in the j th size bin, N_k^{sulfate} represent the number density of background sulfate particles in the k th size bin, and K_{jk} represents the collision rate (*Yue & Deepak [1979]*) between bins j and k . The size distribution of sulfate particles for background (non-volcanic) conditions is taken from a 2-D model calculation by *Weisenstein et al., [1997]*. We assume in equation (2) that Al_2O_3 particles only coagulate with sulfate particles of same or larger size, ensuring that the Al_2O_3 particle is completely coated with sulfate before it is removed. By adopting this assumption, we excluded the possibility that the Al_2O_3 particles may eventually be coated by a series of collisions with smaller sulfate particles. Thus, the results should represent an upper limit.

The collision rate tends to be largest for collisions between small and large particles, because small particles have a high thermal velocity and large particles have a

large cross-section. Therefore, only the small Al_2O_3 particles are removed efficiently under these assumptions. This characteristic is shown in Figure 3, in which the collision removal rate is plotted as function of particle size at 20 km for the equator, 35° N and 70° N. The latitude-altitude cross-section of the reciprocal of the removal rates for 4 seasons are plotted for particles with $0.03 \mu\text{m}$ radius and particles with $0.13 \mu\text{m}$ radius in Figures 4 and 5, respectively. The collision removal is much slower for particles with $0.13 \mu\text{m}$ radius than particles with $0.03 \mu\text{m}$ radius (20 to 30 times slower). The time constant for the $0.13 \mu\text{m}$ case is much larger than the stratosphere residence time of 800 days. Thus, collision removal should have little effects for $0.13 \mu\text{m}$ particles.

2.3 Model Simulations

We used the GISS/UCI 3-D CTM to simulate the quasi-steady state (annually repeating) distribution of Al_2O_3 particulate for the following three cases,

- Baseline: particulate source transported by large scale circulation ignoring sedimentation,
- Case A: particulate source with sedimentation,
- Case B: particulate source with sedimentation and collision removal with the background sulfate particles.

Note that since we assume the Al_2O_3 particles are non-interacting, the baseline case requires only one model run for all sizes of particles. As there are no interactions between Al_2O_3 particles, the simulations in Case A and Case B are run independently for each size bin and the results combined to obtain the surface area.

3. Particulates from Solid Rocket Motors

3.1. Description of Source Function

Malcolm Ko (*AER*) worked with Peter Lohn (*TRW*) to finalize the description of the source for solid fuel rockets. Beiting [1995, 1997] reviewed the measurements through rocket plumes and determined that the particles can be described by a tri-modal distribution specified as follows:

$$n_D(D) = \sum_{i=1}^3 n_i e^{-\gamma_i D} \quad (3)$$

where D is the radius of the particles, n_i is the number density (particle $\mu\text{m}^{-1}\text{cm}^{-3}$) with $n_1/n_2 = 4.65 \times 10^4$, $n_2/n_3 = 10.3$,

$$\begin{aligned} \gamma_1 &= 63.3 \mu\text{m}^{-1} && \text{for } 0.025 \mu\text{m} < D < 0.25 \mu\text{m} \\ \gamma_2 &= 3.13 \mu\text{m}^{-1} && \text{for } 0.25 \mu\text{m} < D < 1.0 \mu\text{m} \\ \gamma_3 &= 0.80 \mu\text{m}^{-1} && \text{for } 1.0 \mu\text{m} < D < 10 \mu\text{m} \end{aligned}$$

If we define $q_{\text{mass}}(\bar{x}, t)$ (gm/cm) as the mass of aluminum oxide deposited per cm vehicle track at location \bar{x} and time t , the number of particles introduced into the model grid box per unit vehicle track $q(D, x, t)$ (in units of particles $\mu\text{m}^{-1}\text{cm}^{-1}$).

$$q(D, \bar{x}, t) = \frac{q_{\text{mass}}(\bar{x}, t)}{\rho_{\text{bulk}}(\bar{x}, t)} \sum_{i=1}^3 n'_i e^{\gamma_i D} \quad (4)$$

where $\rho_{\text{bulk}}(\bar{x}, t)$ is the bulk density of the particles in gm/cc, and the normalization factor n'_i has units of [particles $\mu\text{m}^{-1}\text{cm}^{-3}$]. The n'_i 's are obtained by solving the following equations

$$\begin{aligned} 1 &= \sum_{i=1}^3 n'_i (NV)_i \\ n'_1 &= 4.65 \times 10^4 n'_2 \\ n'_2 &= 10.3 n'_3 \end{aligned}$$

where $(NV)_i$ is the normalized volume given by

$$(NV)_1 = \frac{4\pi}{3} \int_{D=0.025\mu m}^{D=0.25\mu m} e^{-\gamma_1 D} D^3 dD = 1.45 \times 10^{-18} \text{ cm}^3 \cdot \mu\text{m}$$

$$(NV)_2 = \frac{4\pi}{3} \int_{D=0.25\mu m}^{D=1.0\mu m} e^{-\gamma_2 D} D^3 dD = 9.78 \times 10^{-14} \text{ cm}^3 \cdot \mu\text{m}$$

$$(NV)_3 = \frac{4\pi}{3} \int_{D=1.0\mu m}^{D=10.0\mu m} e^{-\gamma_3 D} D^3 dD = 5.82 \times 10^{-11} \text{ cm}^3 \cdot \mu\text{m}$$

The solutions are $n'_1 = 7.85 \times 10^{15}$ [particles $\mu\text{m}^{-1} \text{cm}^{-3}$], $n'_2 = 1.69 \times 10^{11}$ [particles $\mu\text{m}^{-1} \text{cm}^{-3}$], and $n'_3 = 1.64 \times 10^{10}$ [particles $\mu\text{m}^{-1} \text{cm}^{-3}$].

In the Beiting [1995] study, it is assumed that the particles are non-interacting and this tri-modal distribution is preserved as the plume expands. In the calculation, the limited particles are mixed into the grid box. Information from the TRW team indicates that $q_{\text{mass}}(x, t)$ can be specified according to Table 1 for Titan IV launches, with a total emission of 55 tons per launch. The same spatial distribution is used for shuttle launches, but with 100 tons emitted per launch.

Table 1: Vertical Distribution of the Al_2O_3 Particulate Source from each Titan IV Launch

Altitude range (km)	Mass of Al_2O_3 deposited (Ton)	q_{mass} (gm/cm)
15-20	11.6	2.32×10^4
20-25	9.2	1.84×10^4
25-30	9.1	1.82×10^4
30-35	7.4	1.48×10^4
35-40	7.2	1.44×10^4
40-45	5.7	1.14×10^4
45-50	4.8	0.96×10^4

3.2 Model Simulations

The source of Al_2O_3 particulate from SRM includes nine space shuttle launches every year, which deposit 900 ton of Al_2O_3 particulate into the stratosphere, and four Titan launches every year, which deposit 220 ton of Al_2O_3 particulate into the stratosphere. We put the total source of 1120 ton/yr into the model uniformly every day at (20°N, 80°W) with the vertical distribution listed in Table 1 of Section 2. For this study, we decided to input the source in to the model every day uniformly is more suitable than to input a large amount of source at a short period (e.g., in several hours). If we cannot keep the launch schedule the same every year, we think the results of the first scenario are closer to reality.

In this study, we assume that the particulate from the SRM do not interact with each other. They are removed by sedimentation into the troposphere followed by washout; and/or by collision with the background stratospheric sulfate aerosols.

Since both removal rates are size dependent, we must perform separate calculations for each size. In the 3-D model simulations, the particles of Al_2O_3 from SRM are divided into 13 bins covering particle radius from 0.025 μm to 10 μm . The boundaries of bins are $D_{j+1/2}$ with $j = 0-13$. Their values are listed in the first column of Table 2. The size distribution of the Al_2O_3 particulate emitted by SRMs is described by the tri-modal distribution (Equation 3). In the 13 bins, which are used to cover the size distribution of Al_2O_3 particulate for 3-D model simulation, the first 5 bins are in the first mode, bins 6-8 are in the second mode, and the largest 5 bins in the third mode.

The total source (1120 ton/yr) of the Al_2O_3 particles from SRM can be expressed as the sum of sources in each bin,

$$S_{total} = \sum_{j=1}^{13} S_j, \quad (5)$$

$$S_j = \frac{4\pi}{3} \rho_{bulk} C_{\Delta D_j} n_i^* e^{-\gamma_i D} D^3 dD \quad (6)$$

where ρ_{bulk} is the bulk density of the particles (assumed to be 1.7 gm/cc), and

$$\Delta D_j = (D_{j+1/2} - D_{j-1/2}) \quad \text{is the range of the } j \text{ th bin,}$$

$$\text{with } i = 1, n_1^* = 4.79 \times 10^5 \mu\text{m}^{-1}, \gamma_1 = 63.3 \mu\text{m}^{-1}, \quad \text{for } j = 1-5,$$

$$\text{with } i = 2, n_2^* = 10.3 \mu\text{m}^{-1}, \quad \gamma_2 = 3.13 \mu\text{m}^{-1}, \quad \text{for } j = 6-8,$$

$$\text{with } i = 3, n_3^* = 1.0 \mu\text{m}^{-1}, \quad \gamma_3 = 0.8 \mu\text{m}^{-1}, \quad \text{for } j = 9-13.$$

The constant C is obtained by requiring that $S_{total} = 1120 \text{ ton/yr}$ and it is found to be $1.1 \times 10^{19} \text{ yr}^{-1}$. The values of S_j are given in Table 2. They are distributed in altitude as listed in Table 1.

The model computes the mass of the Al_2O_3 particles in each of the 13 bin in each grid box at each time step. As explained in Section 2.3, we considered three cases: the baseline case with no sedimentation and no collision removal, Case A with sedimentation, and Case B with sedimentation and collision removal. Thus, a total of 27 ($2 \times 13 + 1$) simulations are performed.

Since we assume for the baseline case that particles of all sizes are transported at the same rate, the tri-model distribution is preserved and we can use that information to resolve the size within each bin at each subsequent time. This is no longer possible for Case A and Case B because the initial size distribution within each bin will be modified. For the calculation, we assume that the particles within each bin have the same radius given by

$$D_j = (D_{j-1/2} \times D_{j+1/2})^{1/2} \tag{7}$$

the sedimentation velocity (e.g., 1) and the collision rate (e.g., 2) are calculated using D_j .

3.3 Residence Times of Al_2O_3 Particulate from SRM

The residence time is defined as the ratio of the total burden of the Al_2O_3 particles in steady state to the rate of source input. Without sedimentation or collision removal,

the residence time of the Al_2O_3 particles is 2.7 years. With sedimentation, the lifetime of large size particles is reduced markedly. In contrast, the collision removal only affects particles with small radius. With these removal processes operating, the atmospheric lifetimes of particles are functions of particle radius. These are plotted in Figure 6. In the baseline simulation, particles of all sizes have the same source and sink. The only sink is removal at the surface. Therefore, all the particles have the same lifetime of 2.7 years, indicated by the solid line in Figure 6. Note that this is longer than the 2.3 years computed for chlorine (Section 1.3). The reason for this difference is that the source function for chlorine from Prather *et al.*, [1990b] has the chlorine emitted at lower altitudes than the source function in Table 1 for Al_2O_3 . When the sedimentation is added (Case A) the removal of large particles at the surface is accelerated and their lifetime is reduced. The collision removal only affects particles of small size. That is why Case A and Case B differ only for sizes less than $0.13 \mu\text{m}$. The mass-weighted lifetime is about 0.3 years for both Cases A and B since emissions for particles smaller than $0.13 \mu\text{m}$ are small.

3.4 Surface Area of Al_2O_3 Particulate from SRM

The 3-D model calculations generate, $m_j(x)$, the mass of the Al_2O_3 particles in the j th bin in the grid box (x) . The surface area for the j th bin ($a_j(x)$) can be calculated from the mass and the number of Al_2O_3 particles $n_j(x)$ in the j th bin.

$$n_j(x) = m_j(x) / (\rho_{bulk} \times \frac{4\pi}{3} D_j^3), \quad (8a)$$

$$a_j(x) = n_j(x) \times 4\pi D_j^2 = \frac{3m_j(x)}{\rho_{bulk} \times D_j}. \quad (8b)$$

Adding all 13 bins together, we obtain the total local surface area density,

$$a(x) = \sum_{i=1}^{13} a_j(x). \quad (9)$$

The total surface area density around 20 km in January for Case A is plotted in Figure 7, which shows that most Al_2O_3 particles remain in the Northern Hemisphere. The surface

area density is more than four time higher in the northern mid-latitudes than in the Southern Hemisphere. In the longitudinal direction, the distributions of the particle are quite evenly due to the strong zonal wind. The zonally averaged total surface area densities are plotted for four seasons for the Baseline Case, Cases A and Case B in Figures 8, 9 and 10, respectively. The Baseline Case (Figure 8) has the largest surface area density and Case B (Figure 10) has smallest one. This is because that the sedimentation and the collision removal reduce the particle density in the air. In all three cases the total surface area density is smaller in the tropics and subtropics than in the mid-latitudes of the lower stratosphere. The behavior in the tropics matches the shape of the tropopause. The strong convective mixing keeps the particle number density low in the upper tropopause. The order of magnitude of the total surface area density is 10^{-4} ($\mu\text{m}^2/\text{cm}^3$), which is about 3 orders smaller than that of the background aerosol.

The global total surface density is summarized in Table 2.

Table 2. Values for the bin sizes, source strengths and surface area for each bin size for Al_2O_3 particulates from SRM.

Bin Edges (μm)	Radius D_j (μm)	S_j (ton/yr)	Global Surface Area, A_j (10^{12} cm^2)		
			Baseline	Case A	Case B
0.025-0.04	0.03	2.4	3.50	3.38	1.09
0.04-0.06	0.05	4.5	4.22	4.00	1.94
0.06-0.10	0.08	4.3	2.64	2.33	1.60
0.10-0.16	0.13	1.5	0.62	0.44	0.39
0.16-0.25	0.20	0.1	0.035	0.014	0.014
0.25-0.40	0.32	1.5	0.22	0.14	0.14
0.40-0.64	0.51	5.2	0.48	0.26	0.26
0.64-1.02	0.81	12.6	0.73	0.32	0.32
1.02-1.61	1.28	37.3	1.33	0.41	0.41
1.61-2.56	2.03	125.6	2.84	0.57	0.57
2.56-4.06	3.23	295.0	4.28	0.48	0.48
4.06-6.45	5.12	399.2	3.74	0.22	0.22
6.45-10.00	8.13	230.5	1.43	0.04	0.04
Total	----	1120.0	26.06	12.60	7.47

Section 4: Input from Meteorites

When chunks of material enter the mesosphere, they first heated and ablated. The exact sequence of events that lead to the production of micron size particles is rather complicated. We represent this incoming material by a flux of particles deposited at the top of the stratosphere. Dr. Lohn (*TRW*) estimates that at the top of the stratosphere, the mass flux of one-micrometer particle from meteorite is 20-30 ton per year with an assumed bulk density of 2.0 g/cm^3 , this corresponds to a particle flux of 3.6×10^{18} particles/year, or 1.1×10^{11} particles/second. We took the upper limit of the data as input. The input particles are put into the fifth layer from top of the model, which is approximately from 55 km to 60 km, corresponding to the top of the stratosphere. The source is distributed evenly around the globe and input equally everyday.

For the Baseline simulations (no sedimentation and no removal by collision with background aerosols), the calculated total mass is 113.25 ton. Thus, for an inert tracer deposited at around 55-60 km, the residence time is 3.8 years. The corresponding total surface area is $1.70 \times 10^{12} \text{ cm}^2$. When the sedimentation is included in the model, the total mass is 31.5 ton. The calculated residence time for $1 \mu\text{m}$ particles with $\rho_{\text{bulk}} = 2 \text{ gm/cm}^3$ deposited at around 55-60 km is 1.1 years. The total surface area is $4.72 \times 10^{11} \text{ cm}^2$. We did not show the results from the case with collision removal because, for particles of 1 micrometer size, the collision removal is negligible compared with sedimentation (see Figure 6).

The latitude-altitude distributions for 4 seasons of the zonally mean surface area density ($10^{-4} \mu\text{m}^2/\text{cm}^3$) for the Baseline simulation and Scenario A are plotted in Figures 11 and 12. Because of the smaller input (30 tons versus 1120 tons) the total surface area density in the meteor source case is more than one order of magnitude less than that of SRM case. Compared with the SRM source (Figures 12 and 10), the distribution of the total surface area density from the meteor source is more evenly distributed in the two hemispheres because the uniform source distribution assumption. However, there are small seasonal variations which gives higher values in the summer hemisphere. Similar

to the SRM source case, the lowest values of the total surface area density from the meteor source occur near the tropics. The latitude-longitude distribution of the surface area density ($10^{-4} \mu\text{m}^2/\text{cm}^3$) at 20 km from Scenario A of meteor source is plotted in Figure 13. Compared with Figure 7, Figure 13 shows more N-S symmetry and also the values for the total surface area density are much smaller.

Lohn compared the debris population/orbital decay methodology presented here to the results of Zolensky [1989] in 1994 (*Lohn et al., [1994]*). The comparison was reasonable; we calculated particle densities in the stratosphere (as caused by deorbiting debris) that were within a factor of three of the measurements of Zolensky [1989]. This work was described previously in the 1994 report (*Lohn et al., [1994]*).

Section 5: Input from Orbital Debris

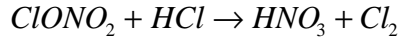
Dr. Lohn (*TRW*) estimates that at the top of the stratosphere, the mass flux of one-micrometer orbital debris objects is 5-10 ton per year with the density of 4.7 g/cm^3 . We took the upper limit of the data as input. As in the Meteor case, 5.1×10^{17} particles/year is put into the fifth layer from top of the model, which is approximately from 55 km to 60 km, corresponding to the top of the stratosphere. The source is distributed evenly around the globe and input equally everyday, as in the Meteor case.

For the Baseline simulations (no sedimentation and no removal by collision with background aerosols), the calculated total mass of the orbital debris in the steady state is 37.8 ton, with a surface area of $2.41 \times 10^{11} \text{ cm}^2$. When the sedimentation is included in the model, the total mass of the orbital debris in the steady state is 6.1 ton. The corresponding residence time is 0.6 years. Note that this is shorter than the residence time of the meteoritic debris because ρ_{bulk} for orbital debris is assumed to be a factor of 2.3 larger. The total surface area is calculated to be $3.86 \times 10^{10} \text{ cm}^2$. Again, we did not include collision removal in the background sulfate because for particles of 1 micrometer size, the collision removal is negligible compared with sedimentation.

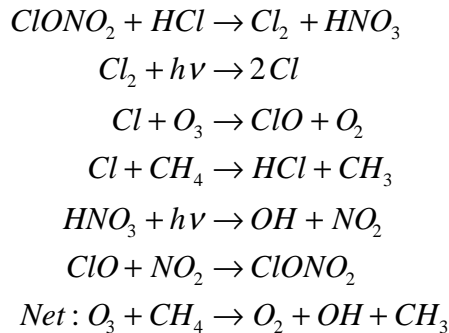
The latitude-altitude distributions for 4 seasons of the zonally mean surface area density ($10^{-4} \mu\text{m}^2/\text{cm}^3$) for the Baseline case and Scenario A are plotted in Figures 14 and 15. They are quite similar to Figures 11 and 12, because the particles from the orbital debris and from the meteor source have the similar source distribution and same sinks. The only difference is that the orbital debris has a smaller source, and the larger bulk density gives even smaller number density. By direct scaling, we expect the surface area to be a factor of 7 smaller even if we ignore the difference in residence time.

Section 6: Estimate of the Effects from Al₂O₃ Particulate on Stratospheric Ozone and the Sulfate Layer

Al₂O₃ particulate may impact stratospheric ozone through heterogeneous reactions occurring on the particle surfaces. The reaction



has recently been measured in the laboratory by Molina *et al.*, [1997] and found to proceed at a reaction probability of ~ 0.2 on aluminum oxide. A similar reaction on polar stratospheric clouds (PSCs) and sulfate aerosol is believed to be responsible for much of the Arctic and Antarctic ozone loss (the “ozone hole”) in springtime. Heterogeneous reaction on Al₂O₃ particles would not be limited to polar regions like the similar reaction on PSCs and, because the reaction rate is not temperature dependent, could occur at all latitudes and seasons, unlike the similar sulfate reaction. The above reaction converts ClONO₂ and HCl, both moderately long-lived chlorine reservoir species, into Cl₂, a very volatile specie that dissociates rapidly in the presence of sunlight into atomic Cl. The chlorine may then lead to ozone removal via the following catalytic cycle



The impact of the Al₂O₃ particulate from SRM on ozone was studied with a 2-D model by Jackman *et al.*, [1998] employing the Molina *et al.*, [1997] rate for ClONO₂+HCl on alumina particles. The calculated ozone impact is extremely small, at most 0.06% ozone depletion in the northern polar region in spring and a global average total ozone change of 0.01% depletion. The surface area density of Al₂O₃ used by Jackman *et al.*, [1998] is greater than our calculated surface area under Case B by factors of 2-10. Therefore we can state that ozone depletion on the global scale due to Al₂O₃ emissions by solid rocket motors at the current shuttle launch rate is less than 0.04% in the northern polar region and ~ 5 x 10⁻⁴ % global average.

Alumina particles from SRM may affect the background sulfate aerosol layer in two ways: by collision of Al_2O_3 particles with the background sulfate layer, increasing its mass and surface area, and by acting as nuclei for $\text{H}_2\text{SO}_4/\text{H}_2\text{O}$ condensation, increasing the number of sulfate aerosol particles and decreasing their mean radius. We may obtain an upper limit estimate of the first effect as follows. We assume that those Al_2O_3 particles that collide with the sulfate particles become coated with sulfate and provide the same surface area for sulfate reactions. Thus, Case A, with no collision removal, and Case B, with collision removal give the difference in surface area. The maximum difference is $4 \times 10^{-4} \mu\text{m}^2/\text{cm}^3$, which may be compared with background sulfate aerosol surface areas of $0.1\text{-}1.0 \mu\text{m}^2/\text{cm}^3$. Thus, the presence of Al_2O_3 particles will increase the surface area of sulfate by less than 0.1%. This is an upper limit since we do not compensate for decrease in sulfate surface area for the sulfate particles that collided with the Al_2O_3 particles.

The second effect can be evaluated by comparing the number of Al_2O_3 particles in the smallest size bin (considered to be the only size likely to act as condensation nuclei) with the total number of sulfate particles per unit volume. The number density of Al_2O_3 particles in bin 1 is plotted in Figure 16. This can be compared with sulfate particle number densities of 1-20 particles per cubic centimeter for those particles greater than $0.025 \mu\text{m}$ radius. We conclude that the impact of Al_2O_3 particles as condensation nuclei for sulfate aerosol is probably small at most latitudes and altitudes, but has the potential to increase the particle number density and surface area in localized regions where number density is otherwise small. It should be noted that the efficiency of Al_2O_3 particles to act as condensation nuclei is unknown, so assessing this effect accurately is not possible at this time.

The study here provides a good indication on the expected effects of rocket launches. A more realistic evaluation will require more careful treatments of the microphysical processes and incorporation of more realistic launch schedules.

References

- Avallone, L.M., and M.J. Prather, "Tracer-tracer Correlation's: Three-dimensional model simulations and comparisons to observations," *J. Geophys. Res.*, *102*, 19,233-19,346, 1997.
- Beiting, E.J., "Predicted Optical Characteristics of Solid Rocket Motor Exhaust Model in the Stratosphere," *J. Spacecraft Rockets*, *34*, 311-317, 1997.
- Beiting, E.J., "Characteristics of Alumina Particles From Solid Rocket Motor Exhaust in the Stratosphere," Aerospace Report No. *TR-95(5231)-8*, The Aerospace Corporation, El Segundo, California, 1995.
- Hall, T.M., and M.J. Prather, "Simulations of the trend and annual cycle in stratospheric CO₂," *J. Geophys. Res.*, *98*, 10,573-10,581, 1993.
- Hall, T.M., and M.J. Prather, "Seasonal evolution of N₂O, O₃, and CO₂: Three-dimensional simulations of stratospheric correlation's," *J. Geophys. Res.*, *100*, 16,699-16,720, 1995.
- Jackman, C.H., D.B. Considine, and E.L. Fleming, "A global modeling study of solid rocket aluminum oxide emission effects on stratospheric ozone," *Geophys. Res. Lett.*, *25*, 907-910, 1998.
- Kasten, F., "Falling speed of aerosol particles," *J. Appl. Meteorol.*, *7*, 944-947, 1968.
- Lohn, P. D., E. Y. Wong, M. J. Molina, M. R. Denison, J. J. Lamb, "The Impact of Deorbiting Space Debris on Stratospheric Ozone," Prepared by TRW for Space and Missile Systems Center, May 31, 1994.
- Molina, M.J., L.T. Molina, R. Zhang, R.F. Meads, and D.D. Spencer, "The reaction of ClONO₂ with HCl on aluminum oxide," *Geophys. Res. Lett.*, *24*, 1619-1622, 1997.
- Prather, M.J., "Numerical advection by conservation of second-order moments," *J. Geophys. Res.*, *91*, 6671-6681, 1986.
- Prather, M.J., M. McElroy, S. Wofsy, G. Russell, and D. Rind, "Chemistry of the global troposphere: Fluorocarbons as tracers of air motions," *J. Geophys. Res.*, *92*, 6579-6613, 1987.

- Prather, M.J., and J.M. Rodriguez, "Antarctic ozone: Meteoric control of HNO₃," *Geophys. Res. Lett.*, 15, 1-4, 1988.
- Prather, M.J., M.M. Garcia, R. Suozzo, and D. Rind, "Global impact of the Antarctic ozone hole: Dynamical dilution with a 3-D chemical transport model," *J. Geophys. Res.*, 95, 3449-3471, 1990a.
- Prather, M.J., M.M. Garcia, A.R. Douglass, C.H. Jackman, M.K.W. Ko, and N.D. Sze, "The Space Shuttle's impact on the stratosphere," *J. Geophys. Res.*, 95, 18,583-18,590, 1990b.
- Rind, D., R. Suozzo, N.K. Balachandran & M.J. Prather, "Climate change and the middle atmosphere, part 1, the doubled CO₂ climate," *J. Atmos. Sci.*, 47, 475-494, 1990.
- Shia, R. L., Y. L. Ha, J. S. Wen, and Y. L. Yung, "Two-dimensional atmospheric transport and chemistry model: Numerical experiments with a new advection algorithm," *J. Geophys. Res.*, 95, 7467-7483, 1990.
- Weisenstein, D.K., G.K. Yue, M.K.W. Ko, N.-D. Sze, J.M. Rodriguez, and C.J. Scott, "A two-dimensional model of sulfur species and aerosols," *J. Geophys. Res.*, 102, 13,019-13,035, 1997.
- Yue, G.K. and A. Deepak, "Modeling of coagulation-sedimentation effects on transmission of visible IR laser beam in aerosol media," *Appl. Opt.*, 18, 3918-3925, 1979.
- Zolensky, M. E., D. S. McKay, and L. A. Kaczor, "A tenfold increase in the abundance of large solid particles in the stratosphere, as measured over the period 1976-1984," *J. Geophys. Res.*, 94, 1047-1056, 1989.

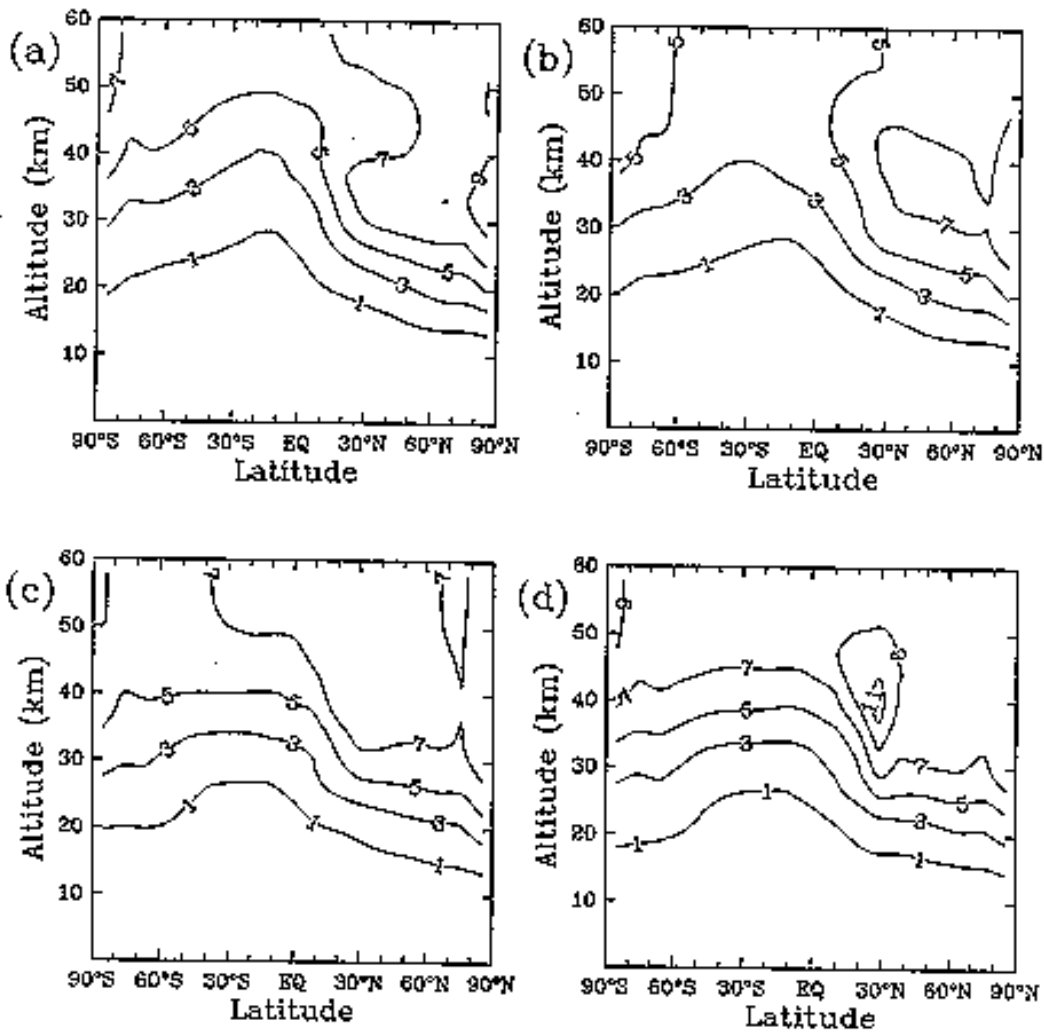


Figure 1A: The simulated steady state zonal mean mixing ratio of Cl (in pptv) due to emission from 9 space shuttle launches annually. It is assumed that the first launch occurs on day 40 of the year with one launch occurring 40 days after. Results are shown for (a) January, (b) April, (c) July, and (d) October. The contour levels are 1, 3, 5, 7, 9, 11 (pptv).

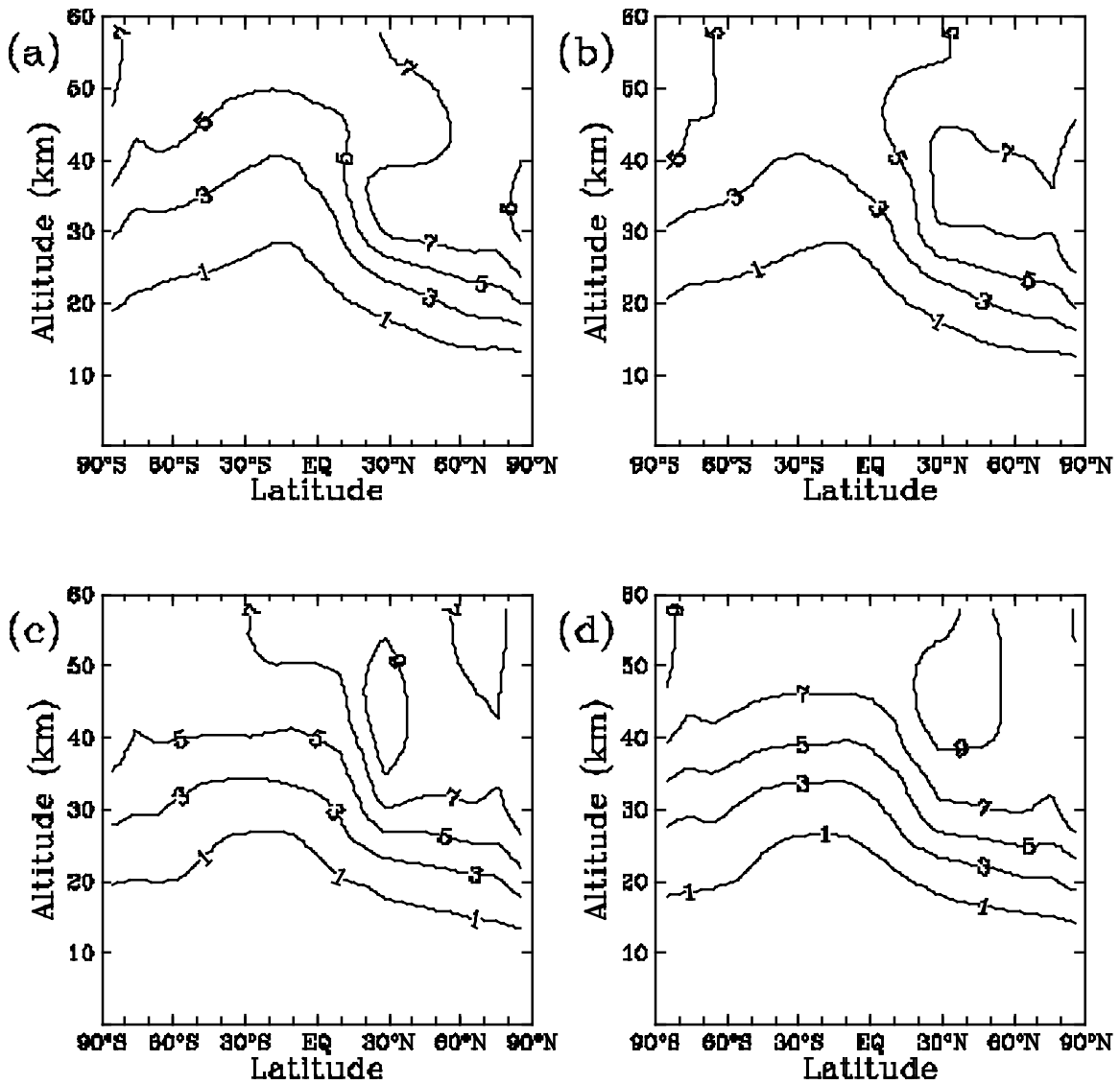


Figure 1B: The simulated steady state zonal mean mixing ratio of Cl (in pptv) due to emission from 9 space shuttle launches annually. The emissions for the nine launches are put into the model at a uniform rate throughout the year. Results are shown for (a) January, (b) April, (c) July, and (d) October. The contour levels are 1, 3, 5, 7, 9 (pptv).

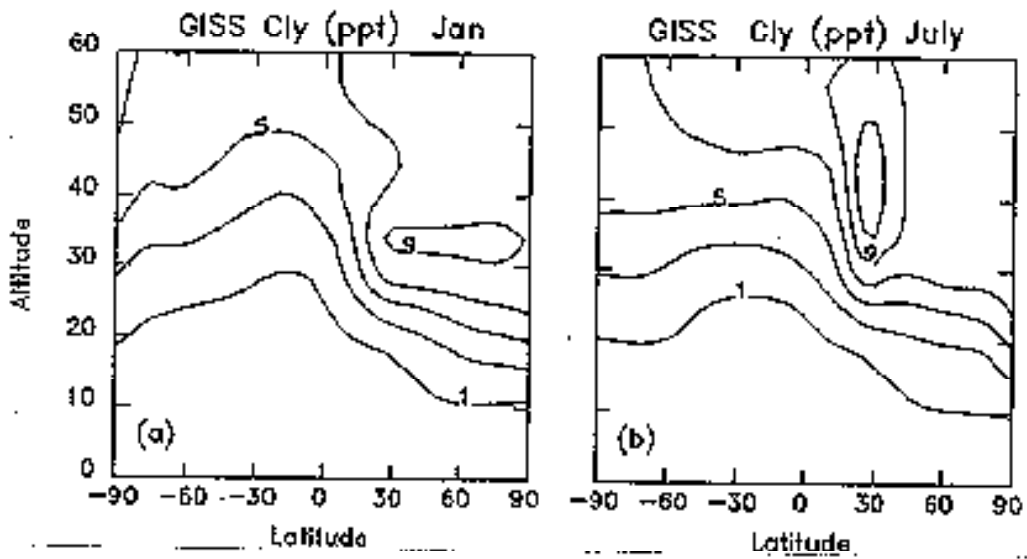


Figure 1C: Model calculated steady state mixing ratio Cl (in pptv) due to emission from nine shuttle and six Titan launches per year as repeated in Prather et.al. (1990b). The total Chlorine input is 725 tons/yr compared to 612 tons/yr used in Figure 1A and 1B. The contour levels are 1, 3, 5, 7, 9, 11 (pptv).

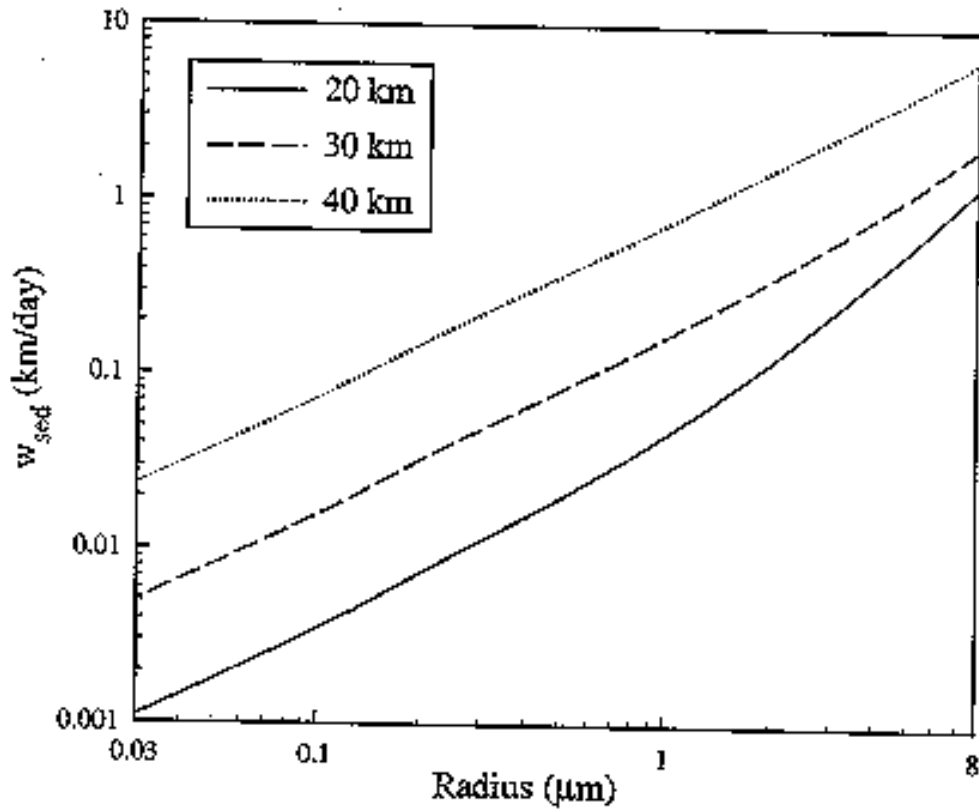


Figure 2: The sedimentation velocity (km/day) of the Al_2O_3 particles from SRM at 20°N as a function of the particle size, assuming a bulk particle density of 1.7 gm/cc . The dotted curve is for particles at 40 km, the dashed curve for 30 km, and the solid curve for 20 km.

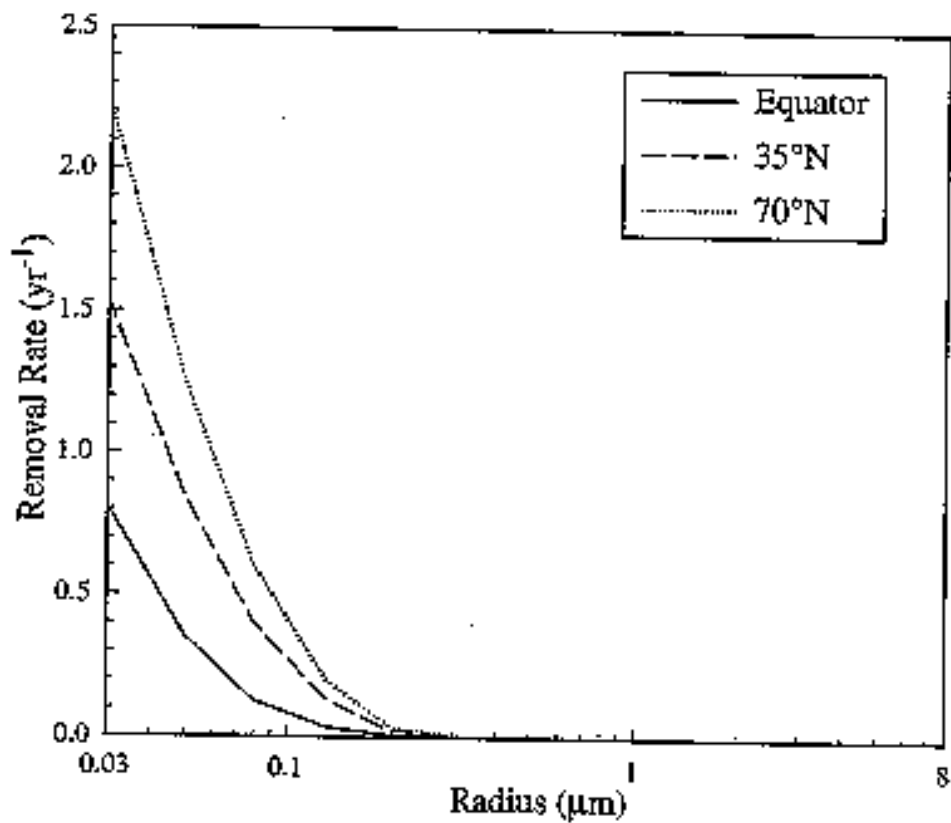


Figure 3: The collision removal rate (yr^{-1}) of the Al_2O_3 particles from SRM at 20 km as a function of particle size. The dotted curve is for particles near 70°N , the dashed curve is for particles near 35°N , and the solid curve is for particles near the Equator.

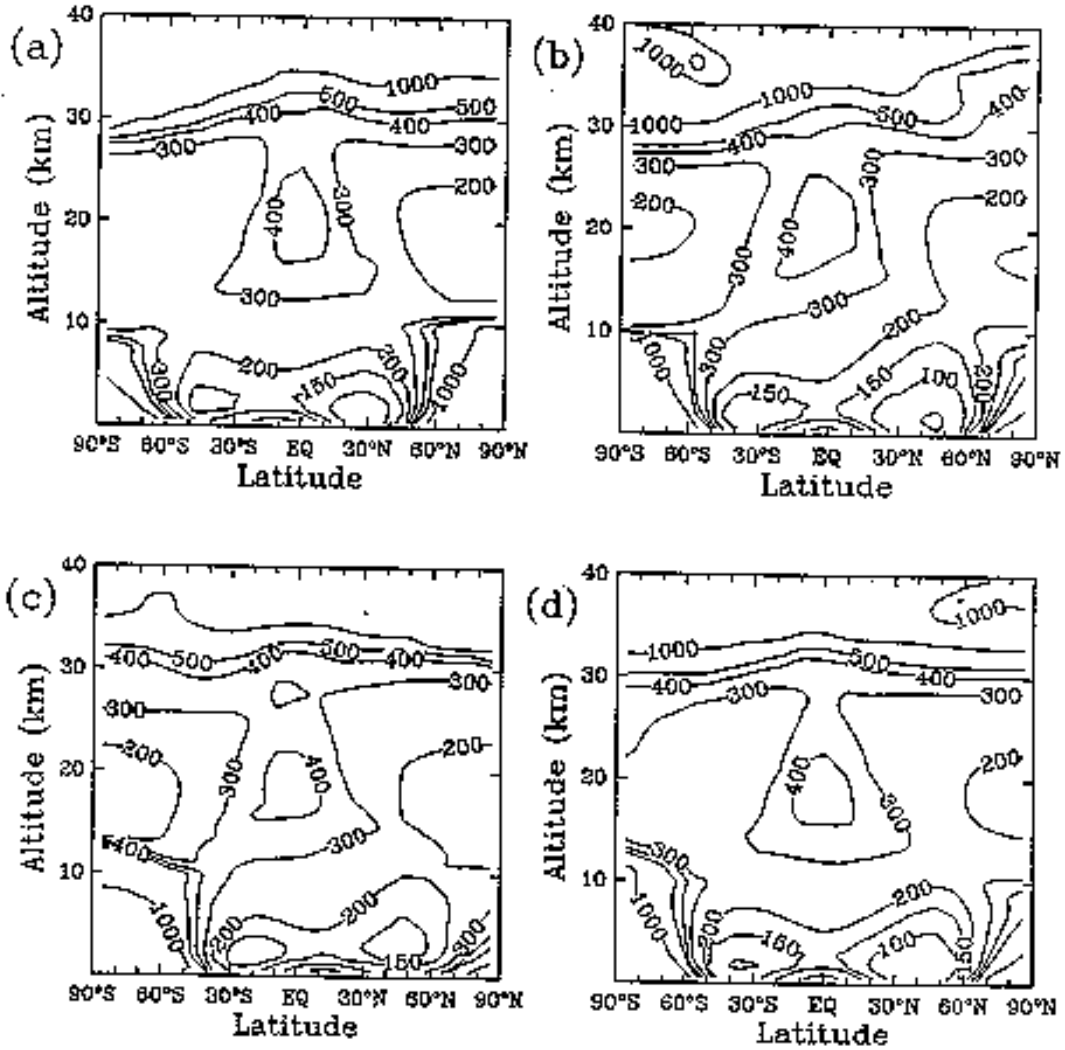


Figure 4: The latitude-altitude distribution of the collision removal time scale (days) of the Al_2O_3 particles in the first bin (radius=0.025-0.04 μm) for (a) January, (b) April, (c) July, and (d) October.

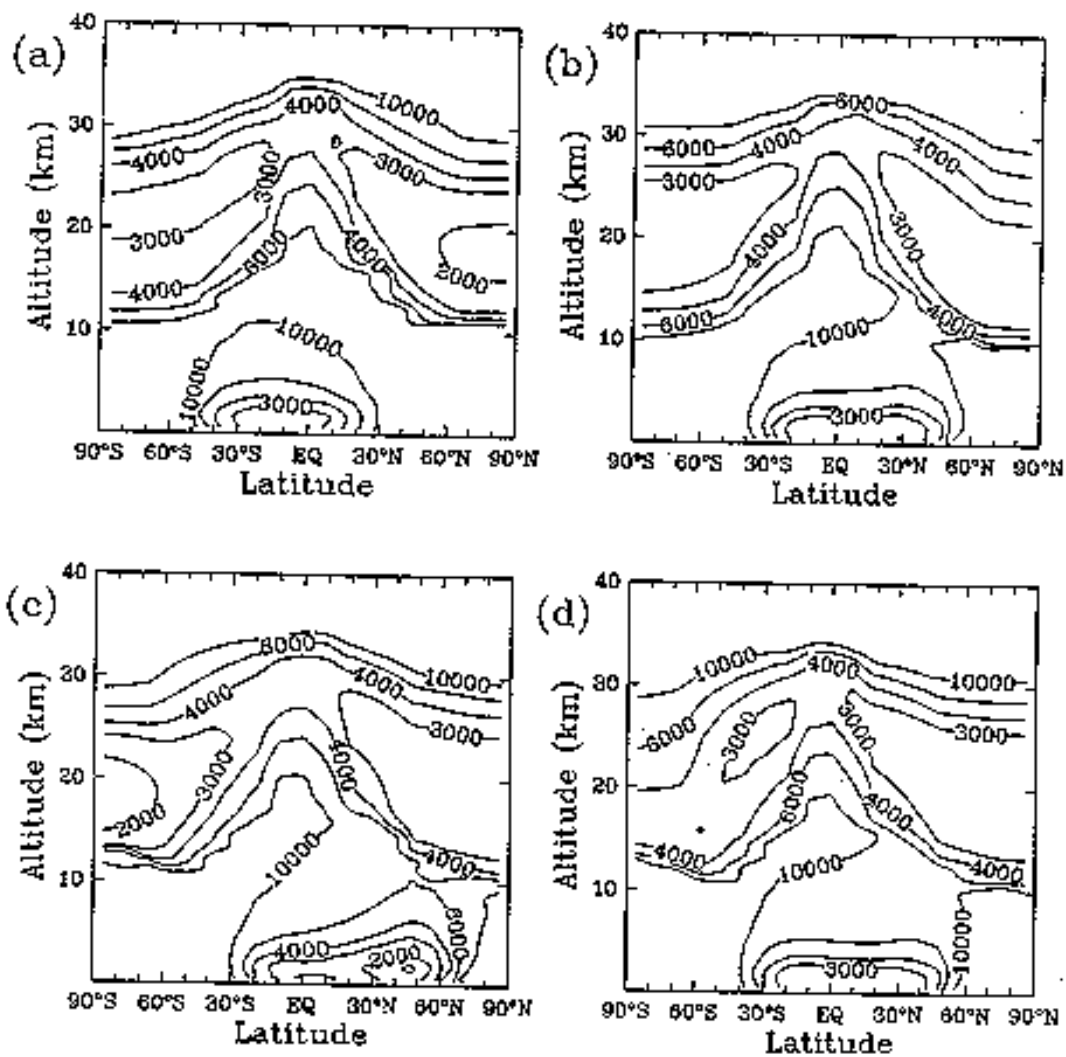


Figure 5: Same as Figure 4, but for the fourth bin (radius=0.10-0.16 μm).

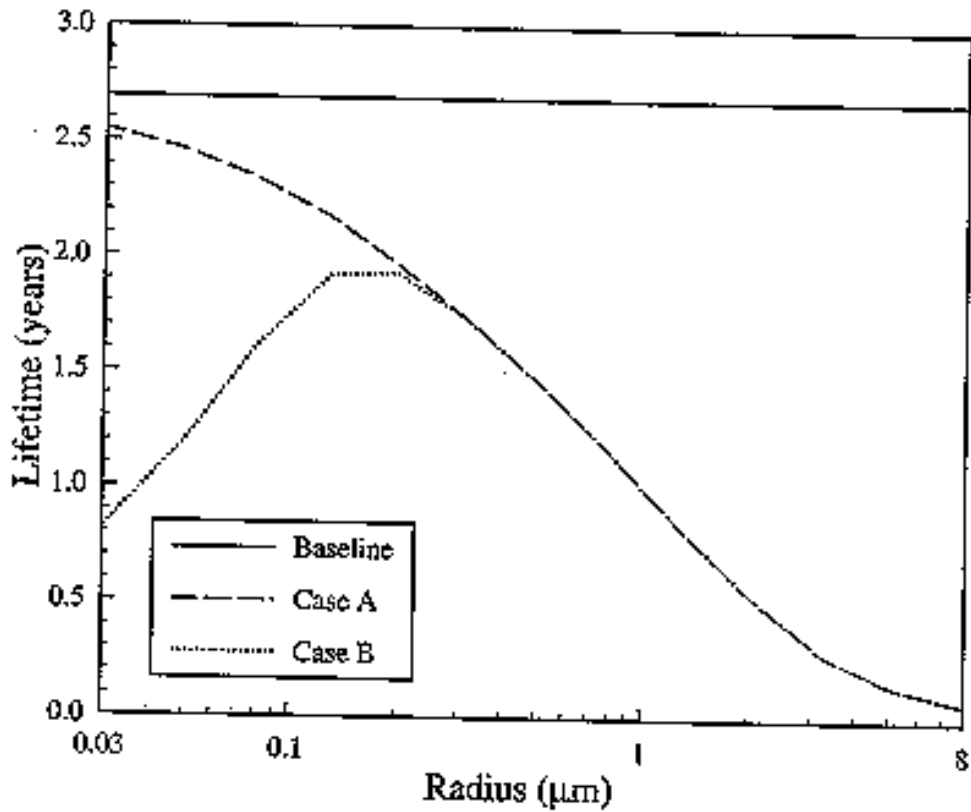


Figure 6: The average residence time (yr) of the Al_2O_3 particles from SRM as a function of particle size. The solid curve is for the Baseline Case, the dashed curve for Case A (sedimentation only) and the dotted curve for Case B (sedimentation and collision removal). Calculation is performed using the size bins as specified in Table 2.

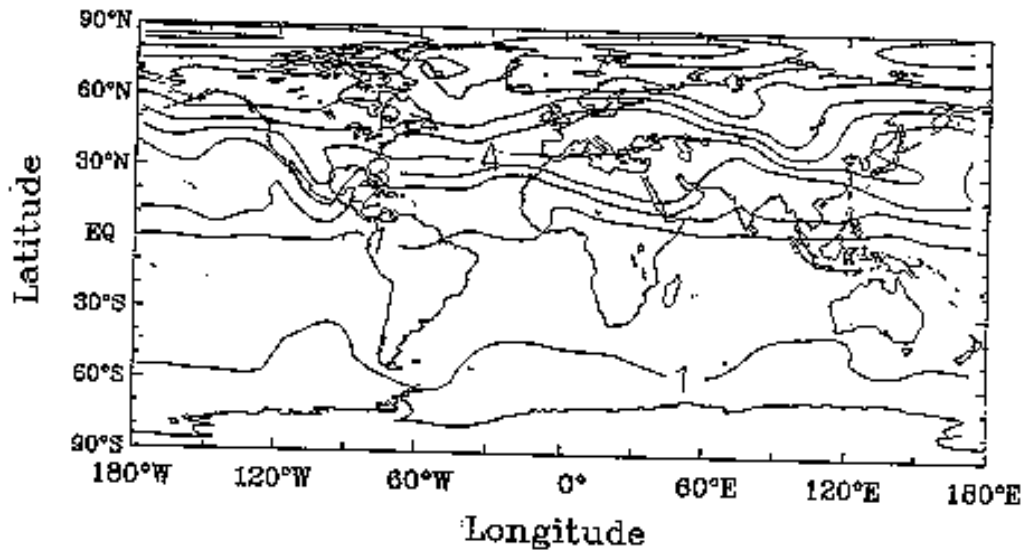


Figure 7: The latitude-longitude distribution of the total surface area density ($10^{-4} \mu\text{m}^2/\text{cm}^3$) of the Al_2O_3 particles from SRM at 20 km in January for Case A (sedimentation only). The contours are from 1 to 9 with increment of 1.

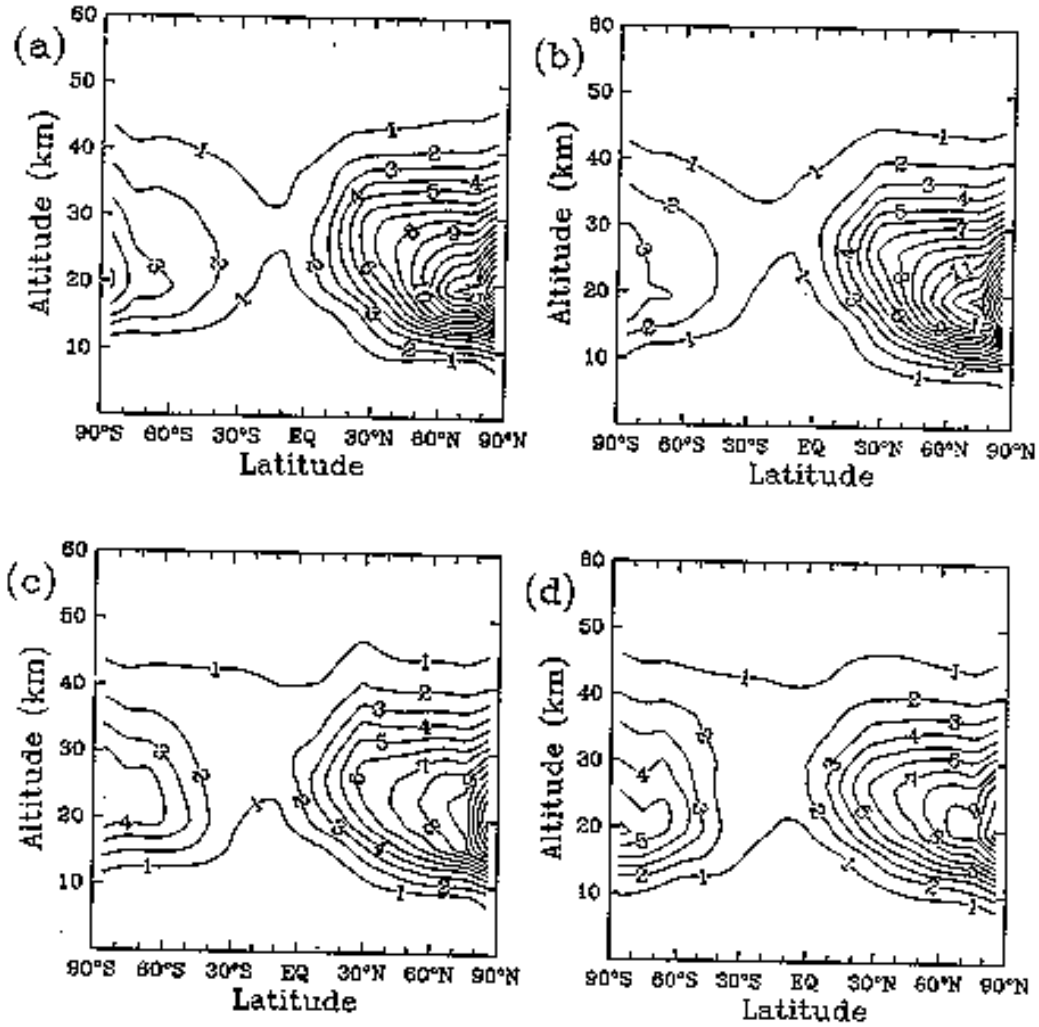


Figure 8: The latitude-altitude distribution of the zonally averaged total surface area density ($10^{-4} \mu\text{m}^2/\text{cm}^3$) of the Al_2O_3 particles from SRM for the Baseline Case for (a) January, (b) April, (c) July, and (d) December. The contours are from 1 to 9 with increment of 1.

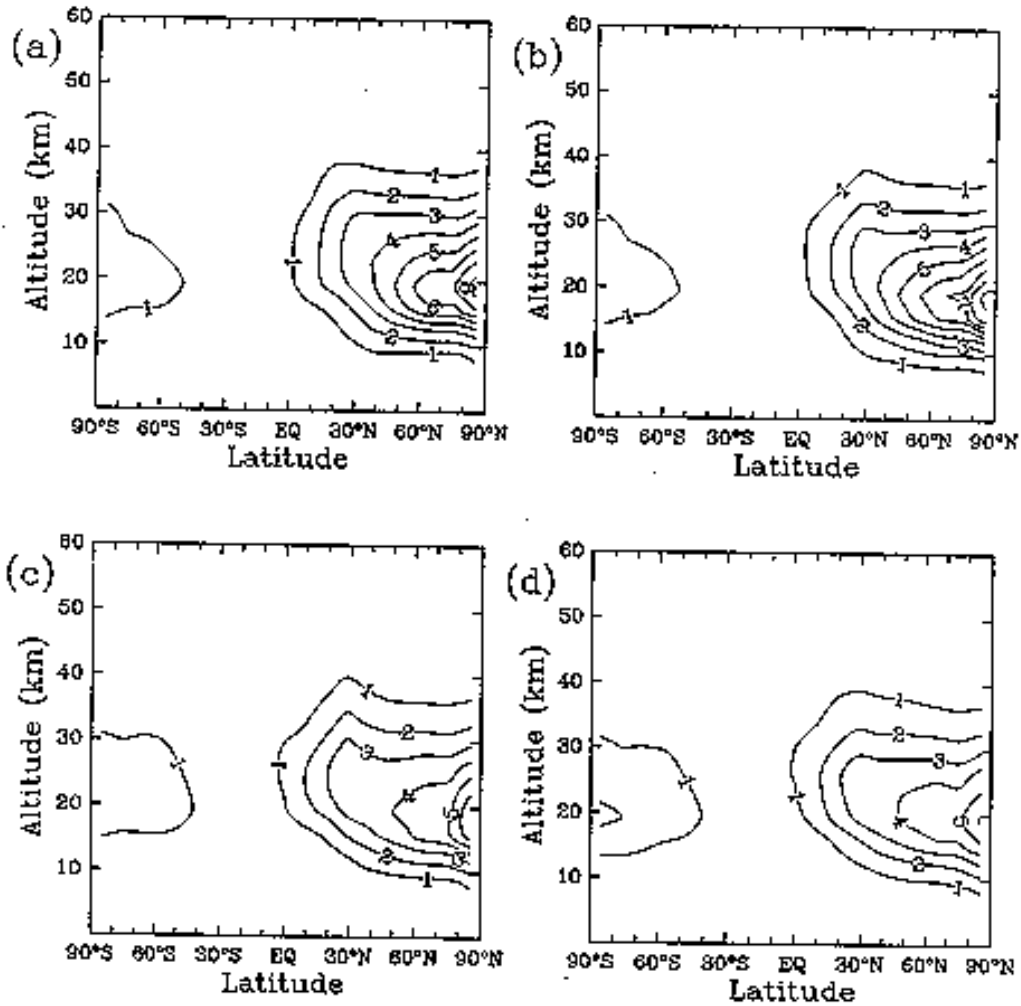


Figure 9: The latitude-altitude distribution of the zonally averaged total surface area density ($10^{-4} \mu\text{m}^2/\text{cm}^3$) of the Al_2O_3 particles from SRM for Case A (sedimentation only) for (a) January, (b) April, (c) July, and (d) December. The contours are from 1 to 9 with increment of 1.

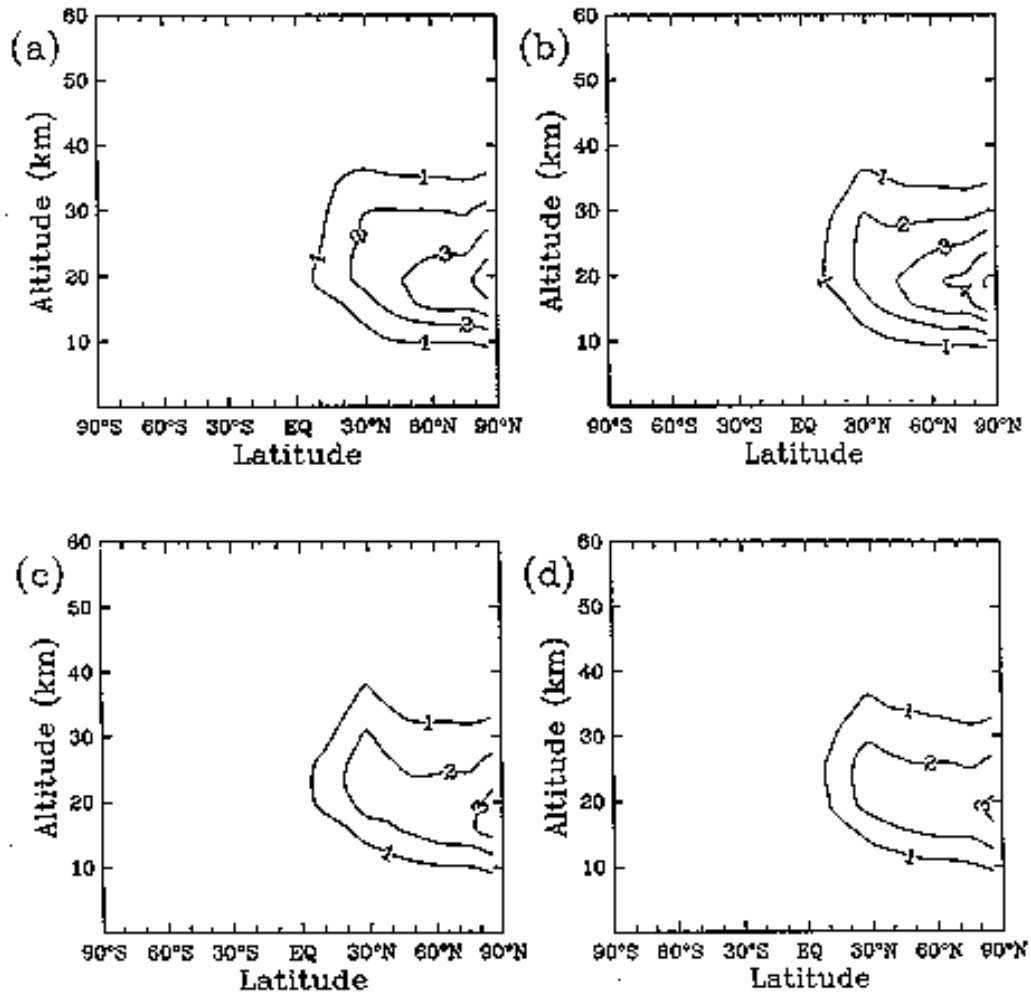


Figure 10: The latitude-altitude distribution of the zonally averaged total surface area density ($10^{-4} \mu\text{m}^2/\text{cm}^3$) of the Al_2O_3 particles from SRM for Case B (sedimentation and collision removal) for (a) January, (b) April, (c) July, and (d) December. The contours are from 1 to 9 with increment of 1.

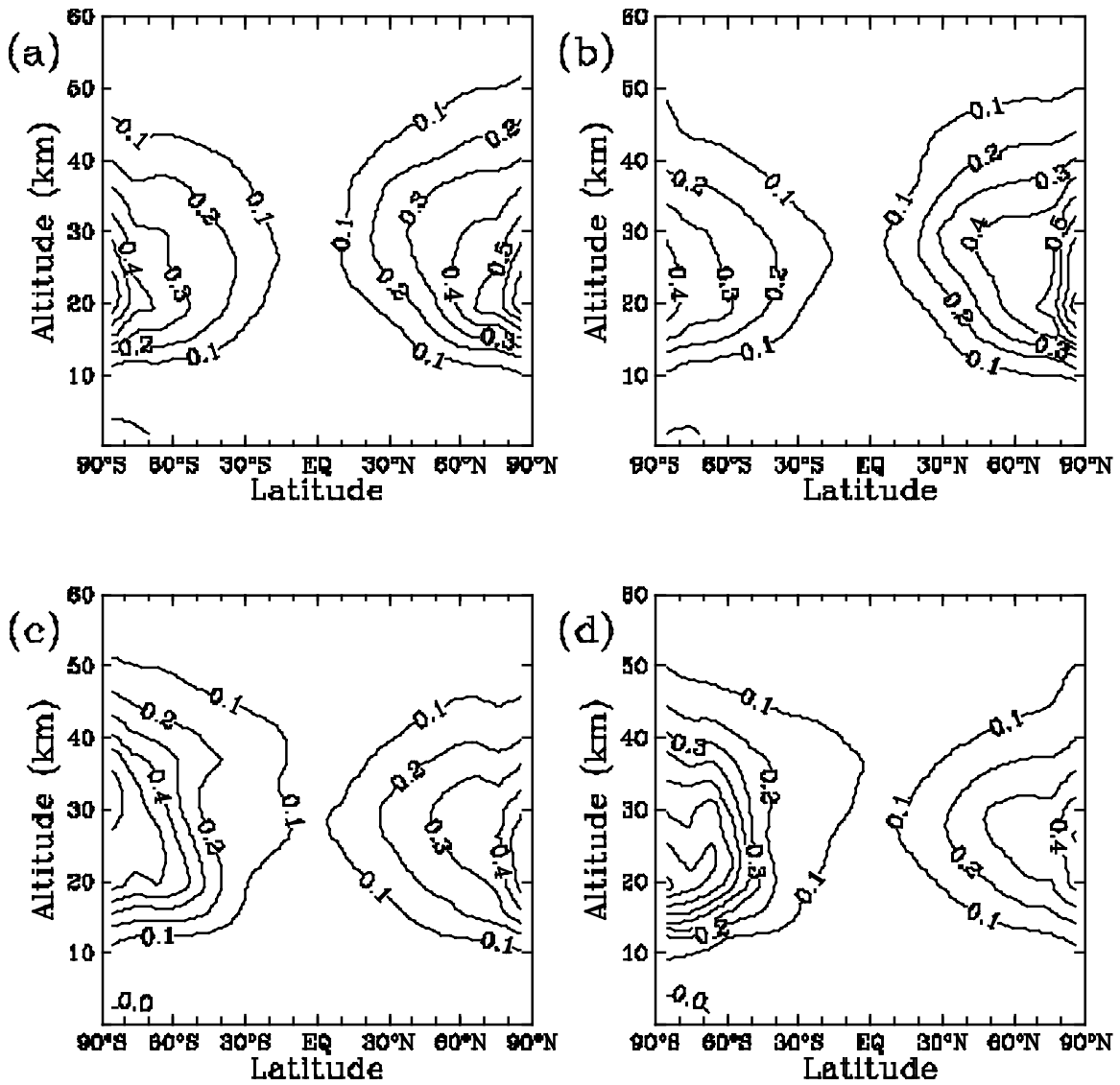


Figure 11: The latitude-altitude distribution of the zonally averaged total surface area density ($10^{-4} \mu\text{m}^2/\text{cm}^3$) of the Al_2O_3 particles from meteor source for the Baseline Case for (a) January, (b) April, (c) July, and (d) December. The contours are 0.1 to 0.9 with increment of 0.1.

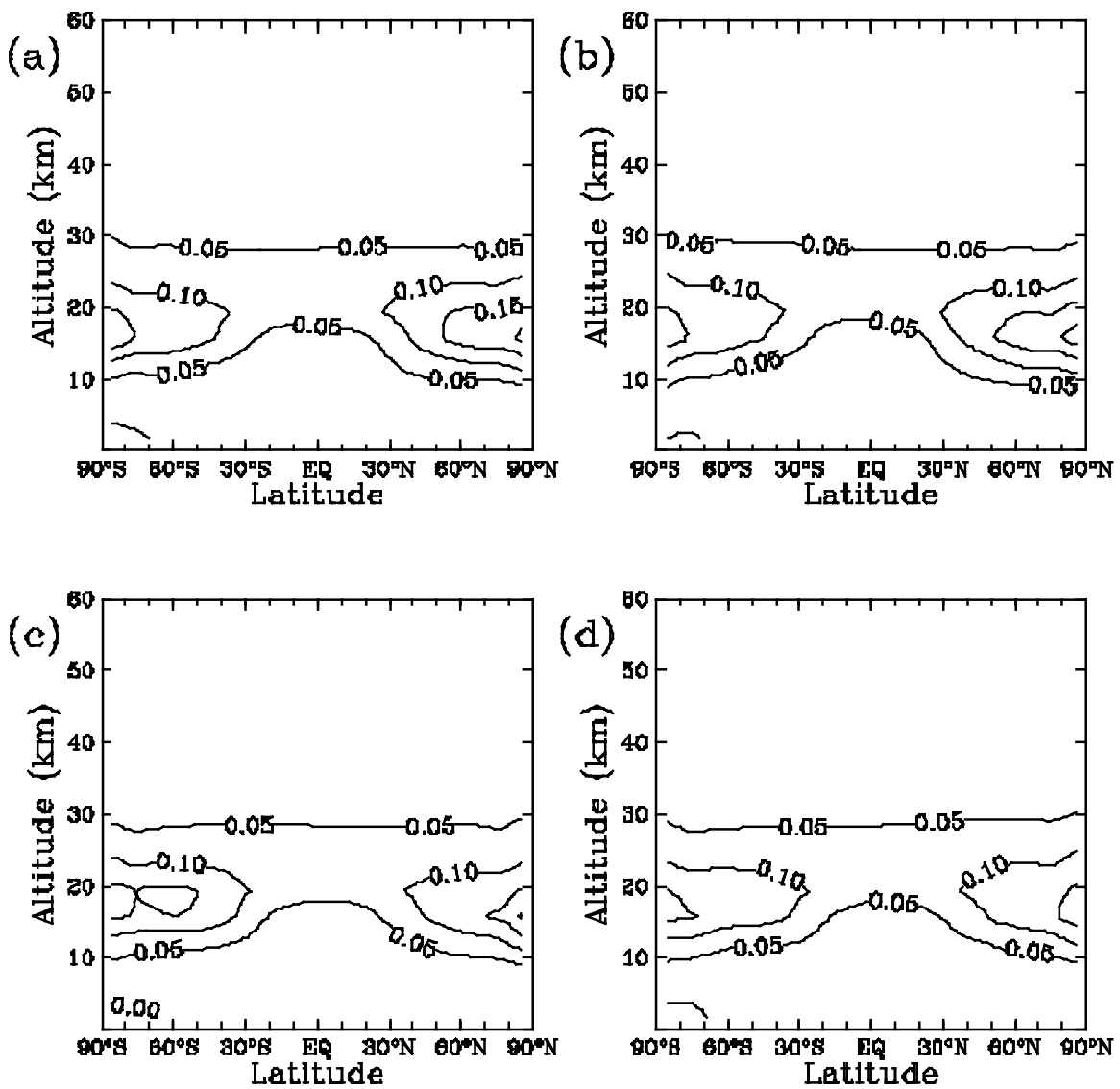


Figure 12: The latitude-altitude distribution of the zonally averaged total surface area density ($10^{-4} \mu\text{m}^2/\text{cm}^3$) of the Al_2O_3 particles from meteor for Case A for (a) January, (b) April, (c) July, and (d) December. The contours are from 0.05 to 0.2 with increment of 0.05.

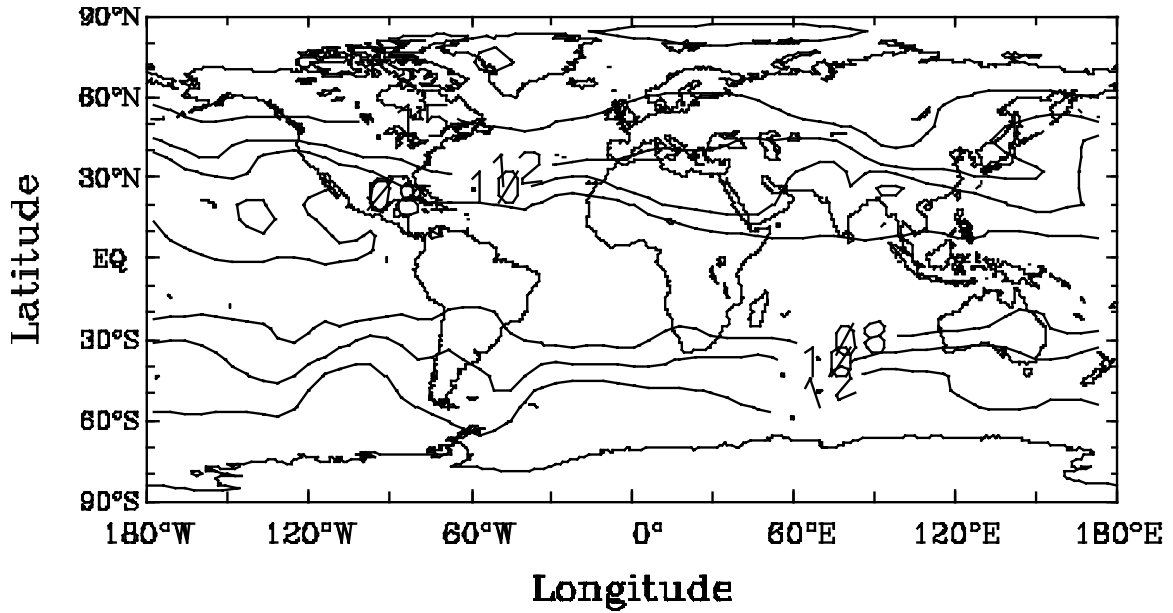


Figure 13: The latitude-longitude distribution of the total surface area density ($10^{-4} \mu\text{m}^2/\text{cm}^3$) of the Al_2O_3 particles from meteor source at 20 km in January for Case A (sedimentation only). The contours are 0.08, 0.1, 0.12, 0.15.

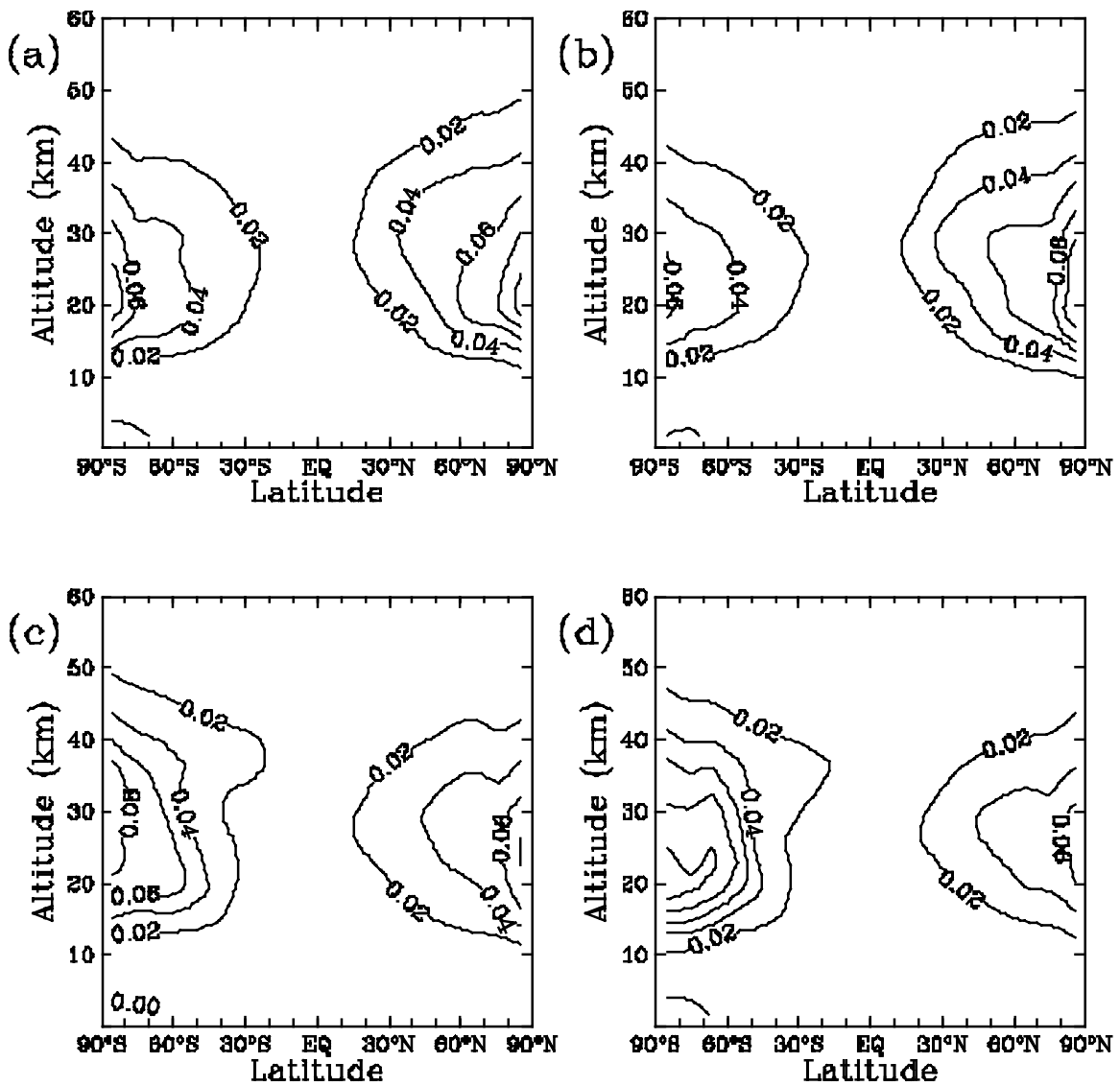


Figure 14: The latitude-altitude distribution of the zonally averaged total surface area density ($10^{-4} \mu\text{m}^2/\text{cm}^3$) of the Al_2O_3 particles from orbit debris for the Baseline Case for (a) January, (b) April, (c) July, and (d) December. The contours are from 0.02 to 0.1 with increment of 0.02.

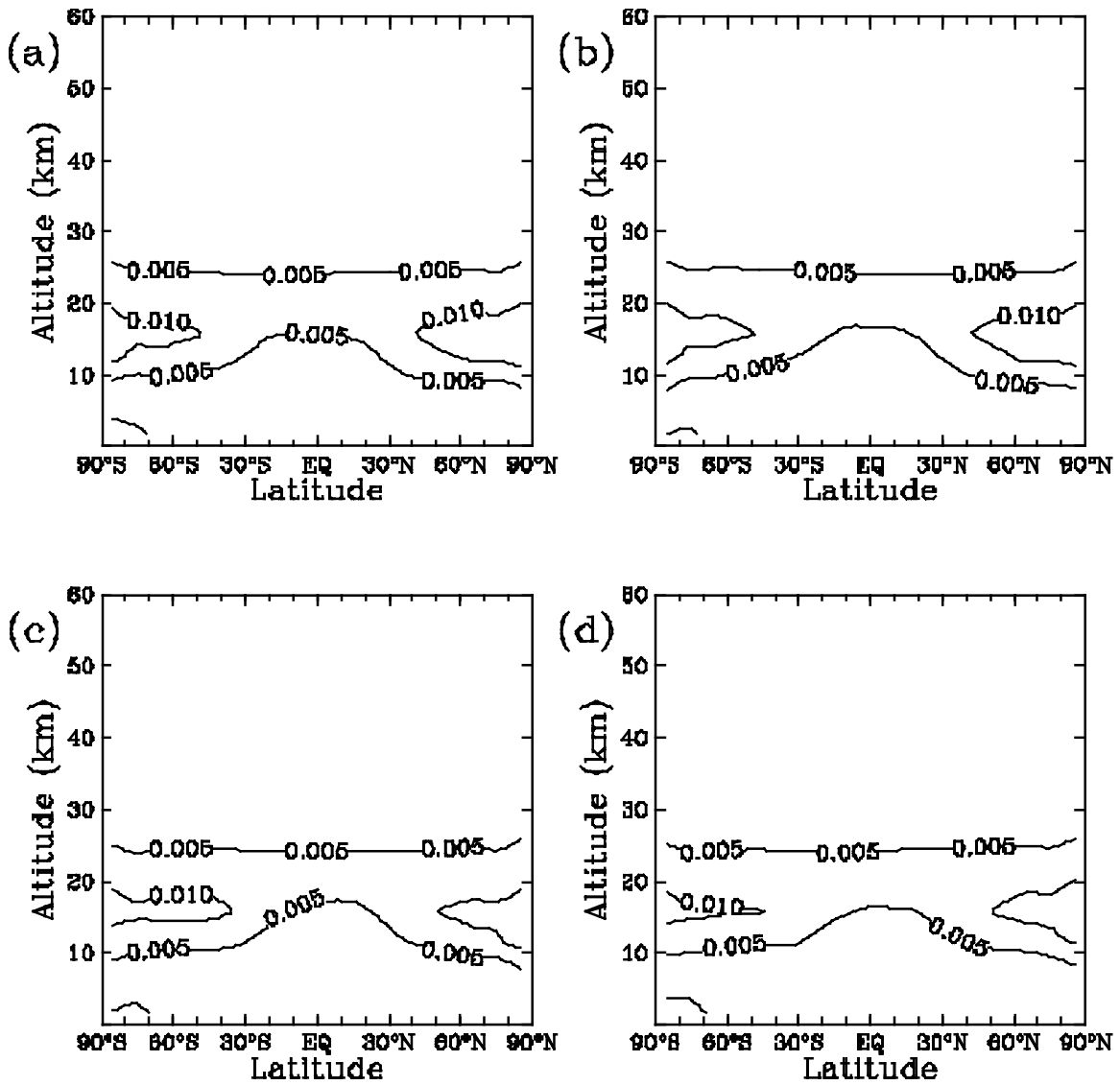


Figure 15: The latitude-altitude distribution of the zonally averaged total surface area density ($10^{-4} \mu\text{m}^2/\text{cm}^3$) of the Al_2O_3 particles from orbit debris for the Case A for (a) January, (b) April, (c) July, and (d) December. The contours are 0.005 and 0.01.

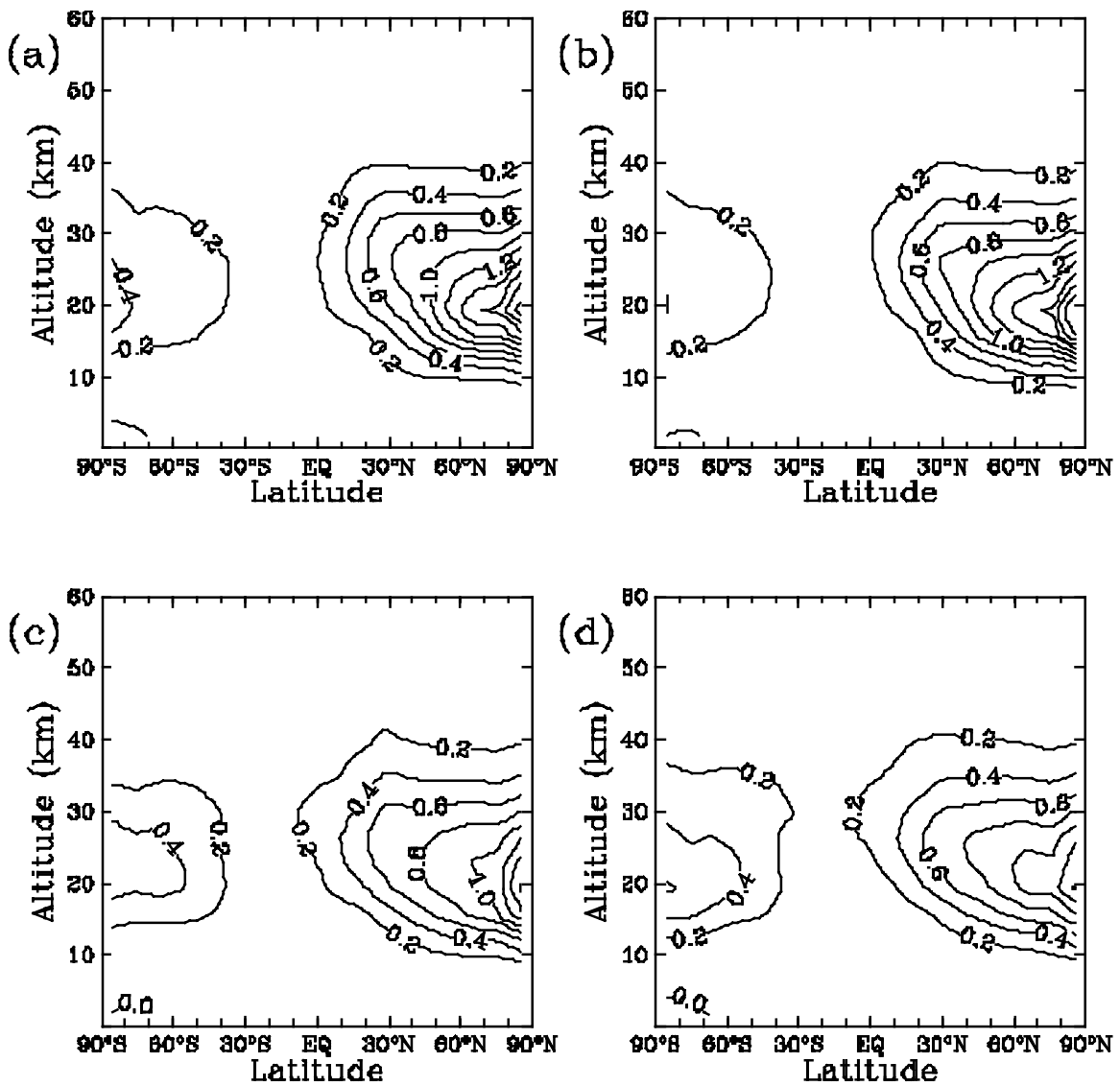


Figure 16: The latitude-altitude distribution of the zonally averaged number density ($10^{-2}/\text{cm}^3$) of Al_2O_3 particles in bin 1 from SRM for the Baseline case for (a) January, (b) April, (c) July, and (d) October. The contours are from 0 to 2 in increments of 0.2.